Mon. Not. R. Astron. Soc. **000**, 000–000 (2014) Printed 1 April 2015 (MN LATEX style file v2.2)

Galaxy Ecosystems: gas contents, inflows and outflows

Zhankui Lu[1⋆], H.J. Mo[1], Yu Lu[2]
[1]*Department of Astronomy, University of Massachusetts, Amherst MA 01003-9305, USA*
[2]*Kavli Institute for Particle Astrophysics and Cosmology, Stanford, CA 94309, USA*

arXiv:1408.2640v2 [astro-ph.GA] 31 Mar 2015

Accepted ..... Received .....; in original form .....

ABSTRACT
We use a set of observational data for galaxy cold gas mass fraction and gas phase metallicity to constrain the content, inflow and outflow of gas in central galaxies hosted by halos with masses between $10^{11}M_\odot$ to $10^{12}M_\odot$. The gas contents in high redshift galaxies are obtained by combining the empirical star formation histories and star formation models that relate star formation rate with the cold gas mass in galaxies. We find that the total baryon mass in low-mass galaxies is always much less than the universal baryon mass fraction since $z = 2$, regardless of star formation model adopted. The data for the evolution of the gas phase metallicity require net metal outflow at $z \lesssim 2$, and the metal loading factor is constrained to be about 0.01, or about 60% of the metal yield. Based on the assumption that galactic outflow is more enriched in metal than both the interstellar medium and the material ejected at earlier epochs, we are able to put stringent constraints on the upper limits for both the net accretion rate and the net mass outflow rate. The upper limits strongly suggest that the evolution of the gas phase metallicity and gas mass fraction for low-mass galaxies at $z < 2$ is not compatible with strong outflow. We speculate that the low star formation efficiency of low-mass galaxies is owing to some preventative processes that prevent gas from accreting into galaxies in the first place.

Key words: galaxies: clusters: general - galaxies: formation - galaxies: interstellar medium - dark matter - method: statistical

1 INTRODUCTION

During the past 10 years, great progress has been made in establishing the connection between galaxies and dark matter halos with the use of various statistical methods (e.g. Yang et al. 2003; van den Bosch et al. 2003; Conroy et al. 2006; Moster et al. 2010; Behroozi et al. 2010; Yang et al. 2012). In particular, empirical models have been developed to describe the star formation and stellar mass assembly histories of galaxies in dark matter halos at different redshifts (e.g. Conroy & Wechsler 2009; Behroozi et al. 2013; Yang et al. 2013; Béthermin et al 2013; Lu Z. et al. 2014a,b). The results obtained all show that star formation is the most efficient in $\sim 10^{12}\,h^{-1}\mathrm{M}_\odot$ halos over a large range of redshift, and that the efficiency drops rapidly towards both the higher and lower mass ends.

The physics that regulates star formation in galaxies has been one of the main research topics in the field of galaxy formation and evolution. The processes that can affect star formation are generally divided into three categories: gas inflow, outflow, and star formation. The low star formation efficiency can either be caused by a reduced gas inflow, a strong gas outflow driven by some feedback processes, or the distribution, thermal and chemical states of the cold gas disk, but how the processes work in detail is still unclear. For high-mass galaxies, the quenching of star formation is believed to stem from the suppression of

⋆ E-mail: lv@astro.umass.edu

© 2014 RAS

gas inflow into the galaxies by processes, such as AGN heating (e.g. Croton et al. 2006), that can heat the gas supply.

For less massive galaxies, one popular scenario is strong gas outflow driven by supernova (SN) explosions and radiation pressure from massive stars (e.g. Dekel & Silk 1986; Oppenheimer & Dave 2008). Because of the relatively shallow potential wells associated with low-mass galaxies, outflows may drive gas out of their host halos, reducing the gas supply for star formation. Preventative scenarios have also been proposed for low-mass galaxies. For example, using a simple analytic model and observational constraints, Bouche et al. (2010) suggests that gas accretion must be suppressed if the halo mass is $< 10^{11}\,\mathrm{M}_{\odot}$. The physical mechanism is uncertain. Heating by the UV background (Ikeuchi 1986; Rees 1986). is found to be effective only in halos with masses below $\sim 10^{10}\,h^{-1}\mathrm{M}_{\odot}$ (e.g. Gnedin 2000). For halos with mass $\sim 10^{11}\,h^{-1}\mathrm{M}_{\odot}$ other heating sources have been suggested, such as gravitational pancaking (Mo et al. 2005), blazar heating (Chang, Broderick & Pfrommer 2011), and galactic winds (e.g. Mo & Mao 2002, 2004; van de Voort et al. 2011).

It is also possible that the low star formation efficiency is caused by a low efficiency of converting cold gas into stars. Indeed, as shown by Krumholz & Dekel (2012) using the metallicity-regualted star formation model developed in Krumholz et al. (2008) and Krumholz et al. (2009), the star formation in very low-mass galaxies can be completely shut off owing to their low metallicities.

To distinguish between the different scenarios, one ultimately needs direct observational constraints on inflow, outflow and the gas distribution in high redshift galaxies. In the absence of such direct observational data at the moment, observational measurements such as the metallicity of the interstellar medium (Tremonti et al. 2004; Erb et al. 2006; Kewley & Ellison 2008), have been used to constrain gas flows and star formation in galaxies (Dalcanton 2007; Erb 2008; Peeples & Shankar 2011; Lilly et al. 2013; Zahid et al. 2014). For instance, using a simple analytic chemical evolution model, Erb (2008) constrained the outflow and argued that the mass loading factor of the outflow should be about unity in order to match the mass-metallicity relation. Using a more sophisticated chemical evolution model that takes into account inflow/outflow of the gas and star formation in the ISM, Lilly et al. (2013) were able to infer, from a set of simple but plausible assumptions, how the mass loading factor of the outflow depends on the mass of host galaxies

In this paper, we construct a model for the galactic ecosystem, which includes the gas content (both atomic and molecular), inflow and outflow of gas and the enrichment of metals. Using current observational data on the gas mass fraction of local galaxies (Peeples & Shankar 2011; Papastergis et al. 2012) and the evolution of gas phase metallicity-stellar mass relation (Maiolino et al. 2008), together with the empirically constrained star formation histories obtained by Lu Z. et al. (2014a), we infer how gas inflow and outflow regulate star formation. The paper is organized as follows. The basic equations that govern the evolution of different components of a galaxy are described in §2. The observational constraints adopted are presented in §3. In §4, we use two optional star formation laws (models) to infer the cold gas mass for galaxies with different masses and at different redshifts. In §5, we constrain the mass and metal exchange between galaxies and their environments to shed light on gas inflow and outflow, using information about the major components of galaxies, such as dark halos, stars, cold gas and metals. Finally we summarize our conclusions and discuss their implications for physically motivated galaxy evolution models in §6.

Throughout the paper, we use a ΛCDM cosmology with $\Omega_{\mathrm{m},0} = 0.273$, $\Omega_{\Lambda,0} = 0.727$, $\Omega_{\mathrm{b},0} = 0.0455$, $h = 0.704$, $n = 0.967$ and $\sigma_8 = 0.811$. This set of parameters is from the seven year WMAP observations (Komatsu et al. 2011). Unless stated otherwise, we adopt the stellar population synthesis model of Bruzual & Charlot (2003) and a Chabrier IMF Chabrier (2003). Solar metallicity is defined as $Z_{\odot} = 0.0142$ in terms of the total metal mass fraction, and as $Z_{\odot,\mathrm{O}} = 0.0056$ in terms of the oxygen mass fraction (Asplund et al. 2009).

2 GALAXY ECOLOGY

2.1 The basic equations

The ecosystem of a galaxy consists of stellar mass ($M_{\star}$), cold gas mass (M_{g}), and metal mass (M_{Z}). The evolution of these components in a galaxy can be described by the following set of equations:

$$\frac{\mathrm{d}M_{\star}}{\mathrm{d}t} = (1-R)\Psi(M_{\mathrm{g}},\, R_{\mathrm{g}},\, Z)\,; \tag{1}$$

$$\frac{\mathrm{d}M_{\mathrm{g}}}{\mathrm{d}t} = \epsilon_{\mathrm{acc}} f_{\mathrm{b}} \dot{M}_{\mathrm{h}} - \dot{M}_{\mathrm{w}} + \dot{M}_{\mathrm{r}} - (1-R)\Psi\,; \tag{2}$$

$$\begin{aligned}\frac{\mathrm{d}M_{\mathrm{Z}}}{\mathrm{d}t} = {} & \epsilon_{\mathrm{acc}} f_{\mathrm{b}} \dot{M}_{\mathrm{h}} Z_{\mathrm{IGM}} \\ & -\dot{M}_{\mathrm{w}} Z_{\mathrm{w}} + \dot{M}_{\mathrm{r}} Z_{\mathrm{r}} \\ & -(1-R)\Psi Z + y\Psi\,.\end{aligned} \tag{3}$$

In this set, Eq. (1) specifies the change in stellar mass, with Ψ being the star formation rate and R being the return mass fraction of evolved stars. Here we make instanteneous recycling approximation, which is reasonable in the redshift range we consider ($0 \leq z \lesssim 2$) because the lifetime of the stars that contribute most of the recycling is short compared to the Hubble time. The star formation rate depends on the mass (M_{g}), distribution (characterized by the size of the cold gas disk, R_{g}), metallicity (Z), and perhaps other proper-

ties of the interstellar medium (ISM), as specified by a star formation law.

Eq. (2) describes the evolution in cold gas mass. The first term on the right hand side is the inflow rate of pristine gas, written in terms of mass accretion rate of the host dark halo, $\dot{M}_{\rm h}$ (see §2.2) multiplied by the universal baryon mass fraction, and a gas accretion efficiency, $\epsilon_{\rm acc}$. In normal circumstances, the efficiency factor $\epsilon_{\rm acc} \leq 1$, and its value may depend on halo mass and redshift. This efficiency may be affected by a variety of physical processes. For instance, if a halo is embedded in a preheated gas, the accretion into the halo may be reduced, making $\epsilon_{\rm acc} < 1$ (Lu Y. & Mo 2007). It is also possible that the halo can accrete gas at a rate of $f_{\rm b}\dot{M}_{\rm h}$, but that certain heating sources such as "radio-mode" AGN feedback in massive halos (Croton et al. 2006) or photoionization heating by local sources (Cantalupo 2010; Kannan et al. 2014), can prevent the coronal gas from cooling, making $\epsilon_{\rm acc} < 1$. $\dot{M}_{\rm w}$ on the right hand of Eq. (2) is gas outflow, and $\dot{M}_{\rm r}$ is the re-accretion rate of the gas mass that has been ejected at earlier times. Finally, the last term on the right hand side is the cold gas consumption rate of star formation.

Eq. (3) describes the chemical evolution. y is the intrinsic metal yield from stars. The metal yield is assumed to be instanteneous, which is a good approximation, because we only consider oxygen produced by short-lived massive stars (§2.3). $Z_{\rm IGM}$, Z, $Z_{\rm w}$, and $Z_{\rm r}$ are the metallicities of the intergalactic medium (IGM), ISM, wind, and the re-accreted material, respectively. Note that we distinguish between the accretion of the pristine gas from the IGM and the re-accretion of the recycled wind material from the galaxy. In general, the metallicity of the wind and recycled material is not necessarily equal to that of the ISM; for example supernova ejecta and stellar wind may directly carry away metals (Mac Low & Ferrara 1999), giving $Z_{\rm w} \geq Z$.

Note that this set of equations is only valid for galaxies with no satellites of comparable masses. Otherwise, the central galaxies may obtain a significant amount of metals by accreting the enriched hot gas of the satellites after halo merger and the ISM once galaxy mergers occur. In this paper we focus only on galaxies with their halo mass in the range $10^{11}\,{\rm M}_{\odot}$ to $2\times10^{12}\,{\rm M}_{\odot}$. In this range the mass of the satellites are typical much smaller than the centrals and major galaxy-galaxy mergers are negligible (Lu Z. et al. 2014b). For more massive galaxies, Eqs 2 and 3 are not sufficient unless the gas and metals brought in by mergers are properly taken into account. Another reason for not to extending to higher halo mass is the limitation of the observational constraints we use. The star formation history 3.1 of more massive galaxies, most of which are quenched, is an average over star formation and quenched galaxies, while the gas phase metallicity 3.2 are limited to star forming galaxies.

Table 1. The oxygen yield as a function of initial stellar metallicity. Results obtained from two different stellar evolution models are presented: P98 is for Portinari et al. (1998) and K06 for Kobayashi et al. (2006). Chabrier IMF (Chabrier 2003) is used in both models.

Model	$Z_{\rm i}=0.0004$	$Z_{\rm i}=0.004$	$Z_{\rm i}=0.02$
P98	0.0168	0.0180	0.0163
K06	0.0134	0.0110	0.0103

2.2 The Halo Assembly History

Our empirical model follows galaxy evolution in the context of realistic halo assembly histories. The assembly of individual dark matter halos is modeled using the halo merger tree generator proposed by Parkinson et al. (2008). This is a Monte-Carlo model based on a modified treatment of the extended Press-Schechter formalism that is calibrated with N-body simulations (see Cole et al. 2008). As shown in Jiang & van den Bosch (2014), the merger trees obtained with this method match those obtained with high-resolution numerical simulations.

Given a halo mass and a redshift, we only follow the average assembly history instead of individual merger trees. The average assembly history is obtained by averaging over the main-branch progenitors of different trees. The intrinsic scatter in both the models and the observational constraints, such as the gas phase metallicity-stellar mass relation and the gas mass fraction-stellar mass relations, is ignored for simplicity.

2.3 The Intrinsic Metal Yield

The intrinsic yield of a simple stellar population can be estimated from the stellar IMF and the adopted stellar evolution model:

$$y = \int_{m_u}^{m_l} mp(m)\phi(m){\rm d}m\,, \qquad (4)$$

where $\phi(m)$ is the IMF and $p(m)$ is the mass fraction of certain metals produced by stars of an initial mass m. Here we adopt two models, one is from Portinari et al. (1998) and the other is from Kobayashi et al. (2006). Table 1 lists the yield of oxygen for different initial metallicities of the stellar population. For both models the oxygen yield depends mildly on the initial stellar metallicity. However, the variance between different models is considerable. The yield predicted by the Kobayashi et al. (2006) model is about 2/3 of that by the Portinari et al. (1998) model. In this paper, we choose the Portinari et al. (1998) model as our fiducial model, since it is consistent with a broad range of stellar evolutions models in the literature (Peeples et al. 2014). The consequence of using a smaller yield will be discussed whenever needed.

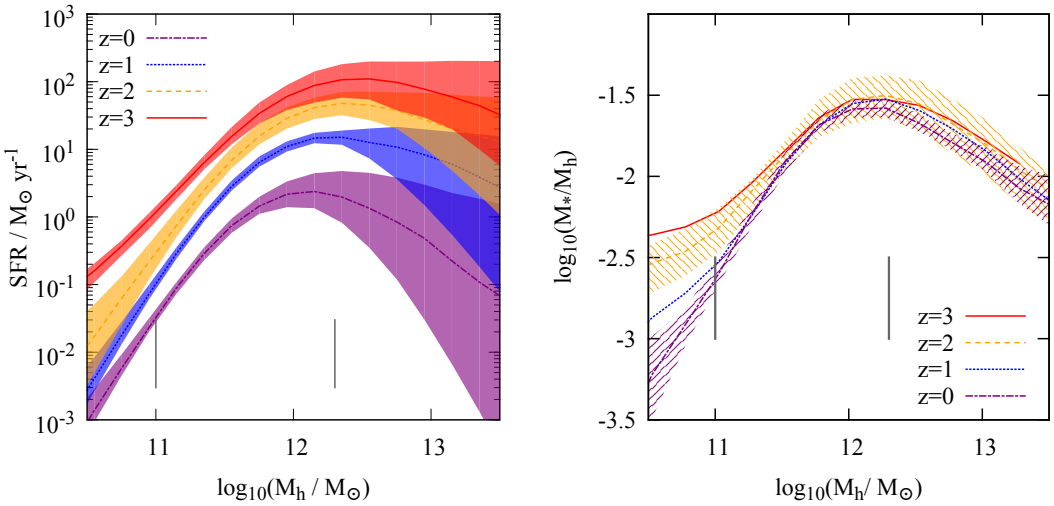

Figure 1. The dependence of SFR (left) and stellar mass to halo mass ratio (right) on halo mass and redshift. The bands represent the 95% credible intervals. The grey vertical lines bracket the halo mass range we focus on in this work.

3 OBSERVATIONAL CONSTRAINTS

3.1 Star Formation History

We make use of the star formation rate (SFR) - halo mass relation obtained by Lu Z. et al. (2014a) and Lu Z. et al. (2014b) as one of our constraints. Specifically, we adopt Model III, in which the star formation rate is written as

$$\Psi = \mathcal{E}\frac{f_{\rm b}M_{\rm h}}{\tau}(X+1)^{\alpha}\left(\frac{X+\mathcal{R}}{X+1}\right)^{\beta}\left(\frac{X}{X+\mathcal{R}}\right)^{\gamma}, \quad (5)$$

where $\mathcal{E}$ is a free parameter that sets the overall efficiency, $f_{\rm b} = \Omega_{\rm b,0}/\Omega_{\rm m,0}$ is the cosmic baryon mass fraction, and $\tau = (1/10\,H_0)\,(1+z)^{-3/2}$ roughly describes the dynamical timescale of halos at redshift z. The quantity X is defined as $X \equiv M_{\rm h}/M_{\rm c}$, where $M_{\rm c}$ is a characteristic mass, and $\mathcal{R}$ is a positive number that is smaller than 1. Hence, the SFR depends on halo mass through a piecewise power law, with α, β, and γ being the three power indices in the three different mass ranges separated by the two characteristic masses, $M_{\rm c}$ and $\mathcal{R}M_{\rm c}$. In this model, the index α is assumed to depend on redshift according to

$$\alpha = \alpha_0(1+z)^{\alpha'}, \quad (6)$$

and γ according to

$$\gamma = \begin{cases} \gamma_{\rm a} & \text{if } z < z_{\rm c} \\ (\gamma_{\rm a}-\gamma_{\rm b})\left(\frac{z+1}{z_{\rm c}+1}\right)^{\gamma'} + \gamma_{\rm b} & \text{otherwise}. \end{cases} \quad (7)$$

Thus γ changes from $\gamma_{\rm b}$ at high-z to $\gamma_{\rm a}$ at low-z, with a transition redshift $z_{\rm c}$.

The model is constrained using the galaxy stellar mass function (SMF) at $z \approx 0$ from Baldry et al. (2012), the SMFs at z between 1 and 4 from Santini et al. (2012) and the z-band cluster galaxies luminosity function by Popesso et al. (2006). The constrained parameters can be found in Lu Z. et al. (2014b). The SFR as a function of halo mass and redshift and the consequent stellar mass to halo mass ratio are shown in Figure 1 for reference, with the bands representing the inferential uncertainty. In the mass range we are interested in here (between the two vertical grey lines), this uncertainty is quite small. We therefore ignore the scatter and use the best fit parameters to characterize the star formation histories.

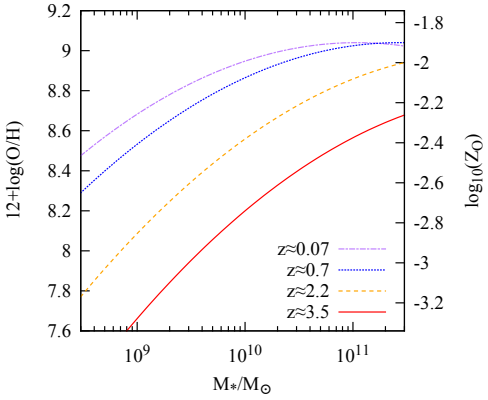

Figure 2. Gas phase metallicity compiled by Maiolino et al. (2008). The y-axis on the right is the corresponding oxygen mass fraction.

3.2 Gas Phase Metallicity

Another observational constraint adopted in this paper is the gas phase metallicity, which is usually measured from the emission lines of the HII regions of star forming galaxies. In this paper, we adopt the metallic-

ity measurements compiled by Maiolino et al. (2008). Figure 2 shows the metallicity-stellar mass relations obtained from their fitting formula. It is important to realize that the metallicity measurements have significant systematic error. For local galaxies the random error in the measurements is only about 0.03 dex (Tremonti et al. 2004), but the systematic uncertainty due to different ways to convert the emission lines into abundances is as large as 0.7 dex (Kewley & Ellison 2008). There are two ways to estimate the metal abundance from such observations: the electron temperature ($T_{\rm e}$) method and the theoretical method. In the T_e method, the ratio between the [OIII]λ4363 auroral line and [OIII]λ5007 is used to estimate the mean electron temperature, which is in turn used to estimate the oxygen abundance (Peimbert & Costero 1969). In the theoretical method, a sophisticated photoionization model is fit to the strong line ratios, such as $R_{23} = ([{\rm OII}]\lambda3737 + [{\rm OIII}]\lambda4959, 5007)/{\rm H}\beta$. Empirical calibrations based on the two methods often show a discrepancy as large as 0.7 dex. Stasinska (2005) pointed out that due to the temperature fluctuation or gradient in high metallicity [$12 + \log_{10}({\rm O/H}) > 8.6$] HII regions, the T_e method can underestimate the metallicity by as much as 0.4 dex. Meanwhile the systematics in the photoionization modeling can be as large as 0.2 dex (Kewley & Ellison 2008). In Maiolino et al. (2008), both of the two methods described above are used to derive the relations between the strong line ratios and metallicity. Specifically, the T_e method is only applied to metal poor galaxies ($12 + \log_{10}({\rm O/H}) < 8.6$) to avoid bias. The empirical calibrations derived in this way cover a large metallicity range and therefore can be applied to galaxies over a large redshift range.

3.3 Gas Fraction in Local Galaxies

In addition, we also include the observations of gas contents in local galaxies compiled by Peeples & Shankar (2011) as a constraint. The data points in Figure 3, which show the total gas mass to stellar mass ratios, are taken from Peeples & Shankar (2011). The binned data points are compiled from several different sources, taken into account HI, helium and molecular hydrogen. Here both the mean relation and the uncertainties, taken as random errors, are used in the data constraint.

4 EVOLUTION OF COLD GAS CONTENT OF GALAXIES

Given the observational constraints for the star formation histories in §3.1 and for the gas phase metallicity in §3.2, we can solve Eq. (1) to obtain the gas mass $M_{\rm g}$ by adopting specific models for the star formation rate and for the structure of the cold gas distribution. In this section, we first introduce the star formation (§4.1) and disk structure (§4.2) models we adopt, we then show the predictions for the cold gas mass in high redshift galaxies (§4.3).

Table 2. Parameters in the Kennicutt-Schmidt model, $A_{\rm K}$ and $\Sigma_{\rm c}$, and in the Krumholz model, $\tau_{\rm sf}$ and c, tuned together with the disk-size parameter, $\mathcal{L}$, to match the gas mass to stellar mass ratio of local galaxies (data points in Figure 3). The second column lists the fitting results and the third column lists the equations which define the corresponding parameters.

parameter	value	
$A_{\rm K}$ $/{\rm M_\odot yr^{-1}pc^{-2}}$	$(2.5 \pm 1.2) \times 10^{-4}$	Eqs. (8) - (9)
$\Sigma_{\rm c}$ $/{\rm M_\odot pc^{-2}}$	9.8 ± 2.6	
$\mathcal{L}$	2.1 ± 0.4	Eq (15)
$\tau_{\rm sf}/{\rm Gyr}$	2.5 ± 0.3	Eqs. (10) - (12)
c	2.6 ± 1.5	
$\mathcal{L}$	3.3 ± 1.0	Eq. (15)

4.1 The Star Formation Models

We consider two different star formation models widely adopted in the literature. The first is the Kennicutt-Schmidt Law (Kennicutt 1998), an empirical relation between the SFR surface density, $\Sigma_{\rm SFR}$, and the cold gas surface density, $\Sigma_{\rm g}$,

$$\Sigma_{\rm SFR} = A_{\rm K} \left(\frac{\Sigma_{\rm g}}{\rm M_\odot pc^{-2}} \right)^{N_{\rm K}} , \qquad (8)$$

where the power index $N_{\rm K} \approx 1.4$, and $A_{\rm K}$ is a constant amplitude. In this model, star formation is assumed to occur only in cold gas disks where the surface density exceeds a threshold $\Sigma_{\rm c}$. Assuming the cold gas disk follows an exponential profile, the total SFR can be obtained as,

$$\Psi = \begin{cases} \frac{2\pi A_{\rm K} \Sigma^{N_{\rm K}} R_{\rm g}^2}{N_{\rm K}^2} \left[1 - \left(1 + N_{\rm K} \frac{r_{\rm c}}{R_{\rm g}} \right) \exp\left(-N_{\rm K} \frac{r_{\rm c}}{R_{\rm g}} \right) \right} \\ \qquad \text{if } \Sigma_0 \geq \Sigma_{\rm c} \\ 0 \\ \qquad \text{if } \Sigma_0 < \Sigma_{\rm c} \, , \end{cases} \qquad (9)$$

where $R_{\rm g}$ is the scale radius of the disk, $\Sigma_0 \equiv \frac{M_{\rm g}}{2\pi R_{\rm g}^2}$ is the surface density at the disk center, and $r_{\rm c} = \ln(\Sigma_0/\Sigma_{\rm c}) \, R_{\rm g}$ is the critical radius, within which star formation can happen. Both $A_{\rm K}$ and $\Sigma_{\rm c}$ are treated as free parameters to be determined by observational constraints.

The other star formation model adopted here is the one proposed by Krumholz et al. (2008, 2009), in which the SFR is assumed to be directly related to

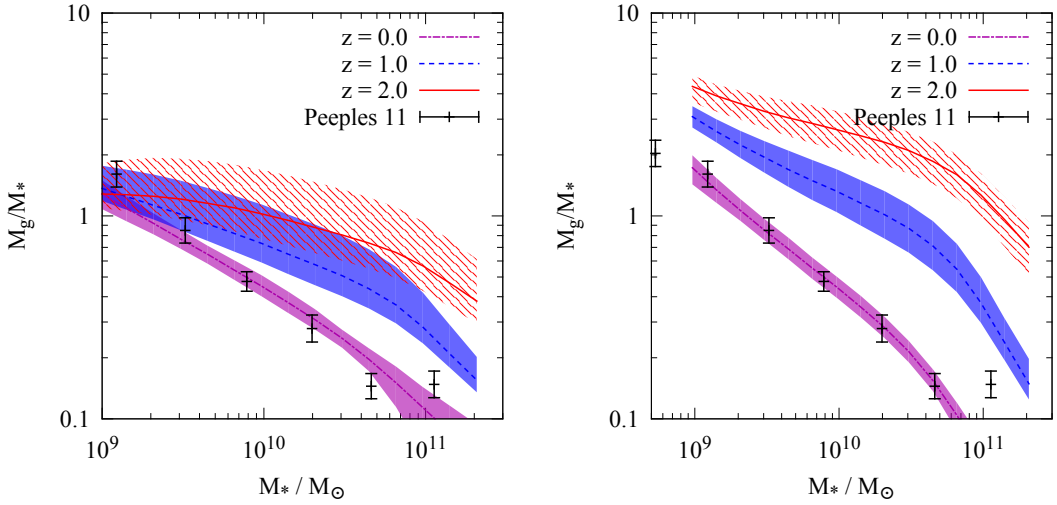

Figure 3. Cold gas to stellar mass ratio as a function of stellar mass at different redshifts calculated using the Kennicutt-Schmidt Law (left) and the Krumholz model (right). The lines are the predictions of the best fitting model in Table 2 and the bands are obtained by marginalizing the uncertainties in the parameters. The data points are compilation of Peeples & Shankar (2011) from different observations of local galaxies.

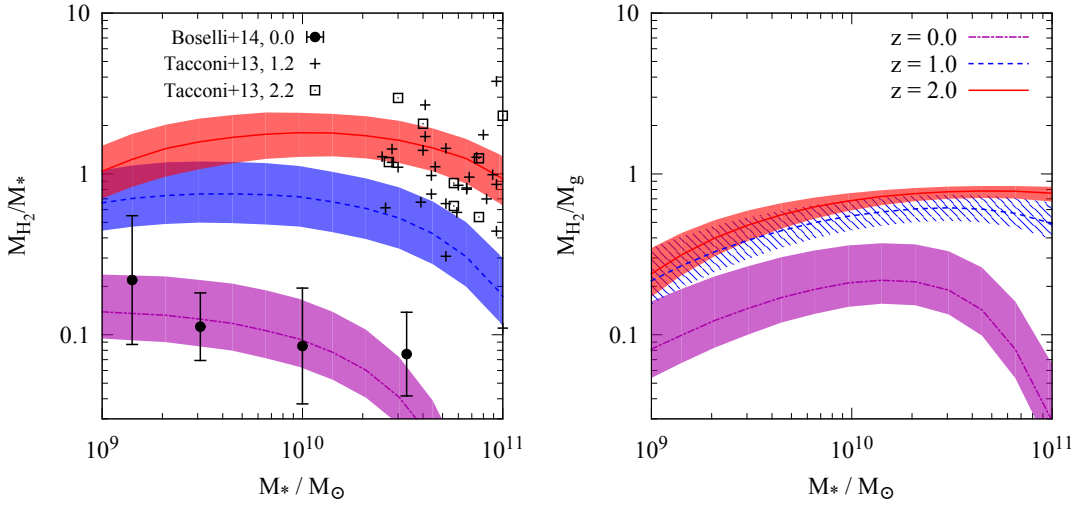

Figure 4. Molecular gas to stellar mass ratio (left), molecular gas to total gas mass ratio (right) as a function of stellar mass, all predicted by the Krumholz model. The lines are the predictions of the best fitting model in Table 2 and the bands are obtained by marginalizing the uncertainties in the parameters. The data points from Tacconi et al. (2013) are individual galaxies the binned data points for local galaxies are from Boselli et al. (2014).

the properties of the molecular cloud:

$$\Sigma_{\rm SFR} = \frac{\epsilon_{\rm ff}}{t_{\rm ff}} \Sigma_{\rm H_2} \,, \tag{10}$$

where $\Sigma_{\rm H_2}$ is the surface density of molecular hydrogen, and $t_{\rm ff}$ is the local free fall time scale. The ratio $\epsilon_{\rm ff}/t_{\rm ff}$ depends on the total gas surface density:

$$\frac{\epsilon_{\rm ff}}{t_{\rm ff}} = \frac{1}{\tau_{\rm sf}} \begin{cases} \left(\Sigma_{\rm g}/85{\rm M}_\odot{\rm pc}^{-2}\right)^{-0.33} & \text{if } \Sigma_{\rm g} < 85{\rm M}_\odot{\rm pc}^{-2} \\ \left(\Sigma_{\rm g}/85{\rm M}_\odot{\rm pc}^{-2}\right)^{0.33} & \text{if } \Sigma_{\rm g} \geq 85{\rm M}_\odot{\rm pc}^{-2} \end{cases}, \tag{11}$$

where $\tau_{\rm sf}$ is a constant, treated as a free parameter. The fraction of molecular gas, $f_{\rm H_2} = \Sigma_{\rm H_2}/\Sigma_{\rm g}$, depends primarily on the surface density and metallicity

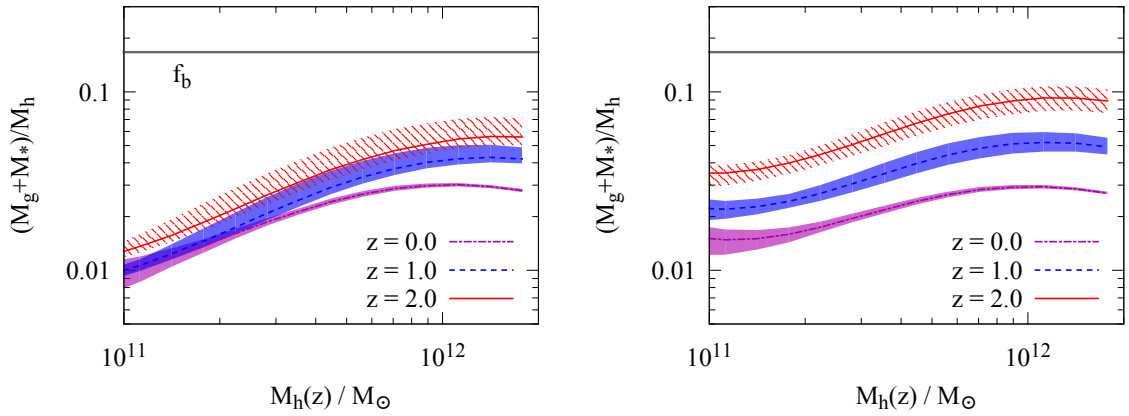

Figure 5. Baryon mass (in both stars and cold gas) to halo mass ratio as a function of halo mass calculated using the Kennicutt-Schmidt Law (left) and the Krumholz Law (right). The horizontal lines indicate the universal baryon fraction. The lines are the predictions of the best fitting model in Table 2 and the bands are obtained by marginalizing the uncertainties in the parameters.

of the cold gas, and is modeled as

$$f_{\rm H_2} = \begin{cases} 1 - \frac{3}{4}\left(\frac{s}{1+0.25s}\right) & \text{if } s \leq 2 \\ 0 & \text{if } s > 2 \end{cases} \quad (12)$$

$$s = \frac{\ln(1 + 0.6\chi + 0.01\chi^2)}{0.6\tau_{\rm c}}$$

$$\chi = 3.1\frac{1 + Z_o^{0.365}}{4.1}$$

$$\tau_{\rm c} = 320 c Z_o \frac{\Sigma_{\rm g}}{\rm g/cm^2}\,.$$

Here Z_o is the metallicity normalized to the solar value, c is a constant treated as a free parameter, and $s = 2$ defines a threshold surface density for the formation of molecular hydrogen. Note that s is roughly inversely proportional to the gas phase metallicity, so that a high metallicity corresponds to a lower surface density threshold.

4.2 Disk Size

To determine the distribution of cold gas, we assume that the cold gas disk follows an exponential radial profile with a disk size proportional to the stellar disk. We estimate the stellar disk size using the empirical size-stellar mass relation obtained by Dutton et al. (2011) for nearby galaxies ($z \approx 0.1$),

$$R_{50} = R_0 \left(\frac{M_\star}{M_0}\right)^\alpha \left[\frac{1}{2} + \frac{1}{2}\left(\frac{M_\star}{M_0}\right)^\gamma\right]^{(\beta-\alpha)/\gamma}\,, \quad (13)$$

where R_{50} is the half light radius of the stellar disk, $\log_{10}(M_0/M_\odot) = 10.44$, $\log_{10}(R_0/{\rm kpc}) = 0.72$, $\alpha = 0.18$, $\beta = 0.52$ and $\gamma = 1.8$. With the assumption that the shape of the relation holds at all redshifts, the time evolution of the disk size is given by the offset

$$\Delta \log_{10}(R_{50}) = 0.018 - 0.44 \log_{10}(1 + z). \quad (14)$$

This redshift dependence is slightly shallower than the more recent observational calibration by van der Wel et al. (2014), which is $\propto (1 + z)^{-0.75}$, but our results are not sensitive to it. As shown by Dutton et al. (2011) the star formation activity typically has a more extended distribution than the stellar disk, with a size about two times the stellar disk, and the relation does not evolve strongly with time. The gas disk is traced by the star formation to some extent. Using a sample of local galaxies that covers a broad range of stellar mass and morphological types, Kravtsov (2013) showed that the sizes of the cold gas disks are typically larger than the stellar disks by a factor of ≈ 2.6. Investigating a semi-analytic model that implements detailed treatments of gas distribution and star formation, Lu Y. et al. (2014) found that the size ratio between the cold gas disk and the stellar disk ranges from 2 to 3 for galaxies with mass in the range considered here. In our model we therefore assume that

$$R_{\rm g} = \mathcal{L} R_\star\,, \quad (15)$$

with $\mathcal{L}$ treated as a free parameter to be tuned along with some other parameters in the star formation models (Table 2) to match the observed gas fraction of local galaxies.

4.3 The Cold Gas Contents

To make use of the models described above, we first calibrate the parameters in the star formation laws and the gas disk size parameter $\mathcal{L}$ using the observed gas mass/stellar mass ratio of local galaxies (Peeples & Shankar 2011). The best fits and the 1 σ uncertainties of the tuned parameters are listed in Table 2. The predicted cold gas contents as functions of stellar mass are shown in Figs. 3 and 4.

Both of the star formation laws can successfully

reproduce the cold gas fraction of local galaxies by tuning the corresponding model parameters. This is in contrast with the finding of Peeples & Shankar (2011) that the Schmidt-Kennicut law fails to match the high gas mass fraction in dwarf galaxies. We find that the critical surface density $\Sigma_{\rm c}$, which was not taken into account in Peeples & Shankar (2011), is crucial in reproducing the steep gas mass fraction-stellar mass relation. Similarly, the Krumholz star formation model also has a critical surface density for molecule formation, which is roughly inversely proportional to the gas phase metallicity [Eq. (12)]. The key difference between the two star formation models is that the critical surface density in the Schmidt-Kennicutt law is a constant, while that in the Krumholz model changes with time and the mass of the host galaxies. According to the observed gas phase metallicity (Figure 2), the critical surface density in Krumholz model increases with redshift. To sustain the same amount of star formation, the gas fraction derived from this model is thus higher than that derived from the Schmidt-Kennicutt law, especially for dwarf galaxies with stellar masses $< 10^9$ M$_\odot$. Using a molecule-regulated star formation model, Dutton et al. (2010) inferred that the gas to stellar mass ratio changes only weakly with time, in contrast to our results shown in Figure 3. The major reason for the difference is that in their model the formation of molecular hydrogen is determined by the total gas surface density, while in the Krumholz model the evolution of metallicity plays a crucial role. Clearly, the gas mass in high redshift galaxies is sensitive to the assumed star formation model, and more models need to be explored and checked with future observations (Popping et al. 2012, 2014).

The Krumholz model also allows us to infer the gas fraction in molecular phase. The left panel in Figure 4 shows the molecular gas to stellar mass ratio. At $z = 0$ the ratio is about 0.1, and it increases by an order of magnitude at $z = 2$. The predictions are consistent with the recent measurements from Boselli et al. (2014) and Tacconi et al. (2013). The right panel shows the molecular gas to total gas mass ratio as a function of stellar mass. At $z > 1$, most of the gas is in the molecular phase.

Regardless which star formation model is adopted, the ratio between the total baryon mass settled in the galaxies and the host halo mass is always much less than the universal baryon mass fraction (see Figure 5). This deficit of baryon mass strongly indicates that star formation models alone cannot account for the low star formation efficiency in low-mass halos. Processes that control the gas exchange between the surrounding medium and galactic medium in forms of gas inflow and outflow must have played a major role. In the following section, we infer limits on the inflow and outflow rates in low-mass galaxies from the constrained star formation histories, cold gas fractions, and metallicity measurements.

5 INFLOW AND OUTFLOW

As described above, the main components of galaxies, such as halo mass $M_{\rm h}$, stellar mass $M_\star$, gas mass $M_{\rm g}$ and mass in gas phase metals $M_{\rm Z} \equiv M_{\rm g} Z$, and their time derivatives can either be obtained directly from observational constraints (§3) or from modeling (§4). In this section, we go a step forward by constraining the terms pertaining to inflow and outflow in Eqs. (2) and (3). As we will see below, these terms cannot be completely determined, but stringent limits can be obtained for them.

To proceed we rewrite Eqs. (2) and (3) in more transparent forms. Since the metallicity of the IGM is expected to be much lower than that of the ISM, we set $Z_{\rm IGM} = 0$ for simplicity. The gas and chemical evolution equations are then reduced to

$$\frac{{\rm d}M_{\rm g}}{{\rm d}t} = \epsilon_{\rm acc} f_{\rm b} \dot{M}_{\rm h} - \epsilon_{\rm loss} \Psi - (1-R)\Psi \,; \quad (16)$$

$$\frac{{\rm d}M_{\rm Z}}{{\rm d}t} = -\epsilon_{\rm loss,Z} \Psi - (1-R)\Psi Z + y\Psi \,, \quad (17)$$

where

$$\epsilon_{\rm loss} \equiv \epsilon_{\rm w} - \epsilon_{\rm r} \equiv \frac{\dot{M}_{\rm w}}{\Psi} - \frac{\dot{M}_{\rm r}}{\Psi} \quad (18)$$

is the loading factor of net mass loss, and

$$\epsilon_{{\rm loss},Z} \equiv \epsilon_{\rm w} Z_{\rm w} - \epsilon_{\rm r} Z_{\rm r} \quad (19)$$

is the loading factor of net metal loss. With some combinations and re-arrangements, Eqs. (16) and (17) can be written as

$$1 - R + \epsilon_{\rm loss} = \epsilon_{\rm acc} \mathcal{E}_{\rm SF}^{-1} \left(1 - \epsilon_{\rm acc}^{-1} \frac{\dot{M}_{\rm g}}{f_{\rm b}\dot{M}_{\rm h}} \right) ; \quad (20)$$

$$\frac{\mathcal{Y}}{Z} = \epsilon_{\rm acc} \mathcal{E}_{\rm SF}^{-1} \left(1 + \epsilon_{\rm acc}^{-1} \frac{M_{\rm g}}{f_{\rm b}\dot{M}_{\rm h}} \frac{\dot{Z}}{Z} \right) , \quad (21)$$

where $\mathcal{E}_{\rm SF} \equiv \Psi/(f_{\rm b}\dot{M}_{\rm h})$ is the star formation efficiency, which is constrained with the empirical model of Lu Z. et al. (2014a), and

$$\mathcal{Y} \equiv y - \epsilon_{\rm w} (Z_{\rm w} - Z) + \epsilon_{\rm r} (Z_{\rm r} - Z) \,. \quad (22)$$

This quantity can be interpreted as the "net yield". For instance, the second term $\epsilon_{\rm w} (Z_{\rm w} - Z)$ represents the metals taken away by the galactic wind without being mixed with the ISM.

The above equations are general and are used to make model predictions to be described below. Before presenting the results, let us look at these equations under certain approximations, which will help us to understand the results obtained from the full model and to make connections to results obtained earlier under similar approximations. Since $M_{\rm g}$ is typically much smaller than $f_{\rm b} M_{\rm h}$, as shown in Figure 5, $\dot{M}_{\rm g}/(f_{\rm b}\dot{M}_{\rm h})$ in Eq. (20) and $[M_{\rm g}/(f_{\rm b}\dot{M}_{\rm h})](\dot{Z}/Z)$ in Eq. (21) are expected to be much less than unity. Thus, if $\epsilon_{\rm acc}$ is of the order of unity or $\epsilon_{\rm acc} \gg [M_{\rm g}/(f_{\rm b}\dot{M}_{\rm h})](\dot{Z}/Z)$ and $\epsilon_{\rm acc} \gg \dot{M}_{\rm g}/(f_{\rm b}\dot{M}_{\rm h})$, the

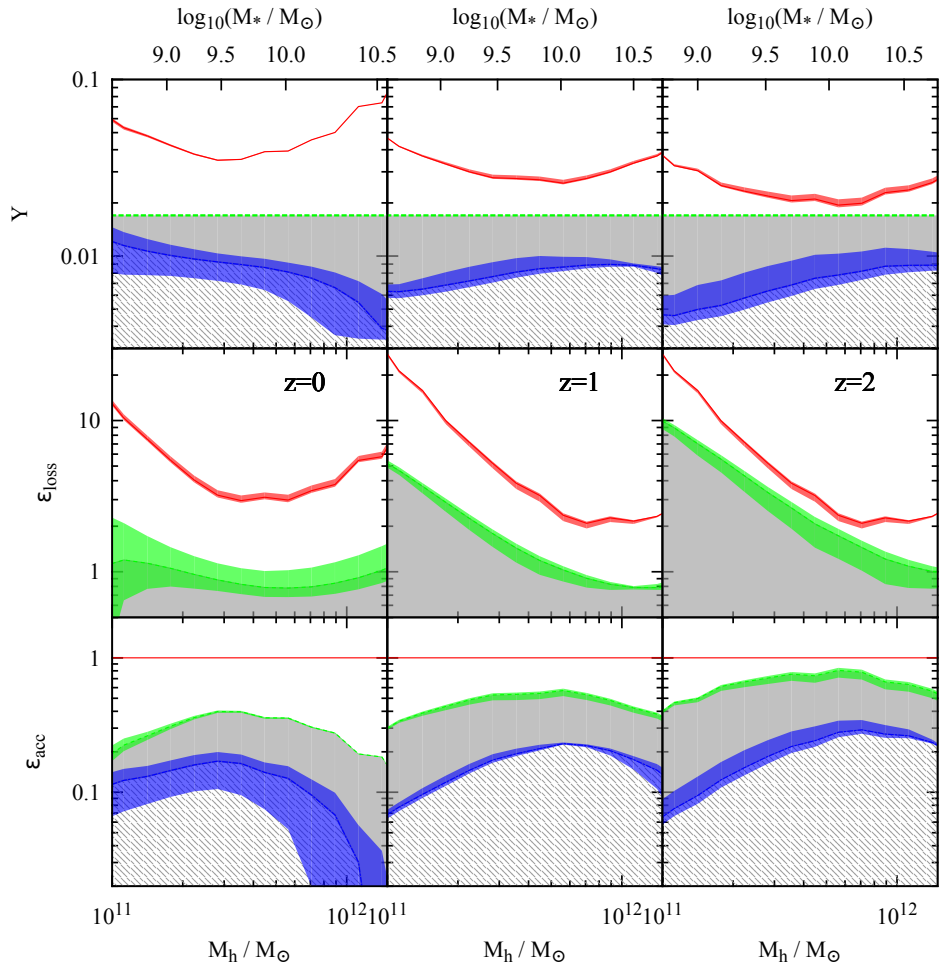

Figure 6. The red lines (bands) are obtained by assuming $\epsilon_{\rm acc} = 1$, i.e. galaxies accrete at the maximum rate. The green lines (bands) are obtained by assuming $\mathcal{Y} = y$, which means full mixing of newly produced metals in the ISM, and no recycling or instanteneous recycling of the ejected material. The blue lines (bands) are obtained by setting $\epsilon_{\rm loss} = 0$. The areas that are not shaded are forbidden by the observational constraints. Here the Kennicutt-Schmidt law is assumed. The lines are the predictions of the best fitting model in Table 2 and the bands are obtained by marginalizing the uncertainties in the parameters. The hatched regions correspond to constraints when $\epsilon_{\rm loss}$ is allowed to be negative (see text).

above equations can be simplified to

$$1 - R + \epsilon_{\rm loss} \approx \epsilon_{\rm acc}\mathcal{E}_{\rm SF}^{-1}\,; \quad (23)$$

$$\frac{\mathcal{Y}}{Z} \approx \epsilon_{\rm acc}\mathcal{E}_{\rm SF}^{-1}\,. \quad (24)$$

In this case, the star formation efficiency ($\mathcal{E}_{\rm SF}$) and the chemical evolution is completely determined by the gas exchange between the galaxies and their environment, independent of the gas content of the galaxy. The choice of star formation law is also not important unless it gives a gas mass that is comparable to $f_{\rm b}M_{\rm h}$. This set of equations is basically equivalent to equations (16) and (18) in Dave et al. (2012), which are derived directly from the assumption that gas inflow, outflow and consumption by star formation are in equilibrium. This approximate model was adopted by Henry (2013) to evaluate the plausibility of different wind models (and models with no wind). We caution, however, that this simplified model is not general, and is only valid under the assumptions described above.

5.1 Models with strong gas outflow

A commonly adopted assumption in galaxy formation models is that halos accrete baryons at the maximum rate, $f_{\rm b}\dot{M}_{\rm h}$. For halos with mass below $10^{12}\,{\rm M}_\odot$, where the radiative cooling timescale is always shorter than halo dynamical time, the gas accretion onto the central galaxy is also expected to follow the halo accretion. We test the consequence of this basic assumption using our constrained model.

Setting $\epsilon_{\rm acc} = 1$, i.e. assuming galaxies are accreting at the maximum rate, we can calculate the

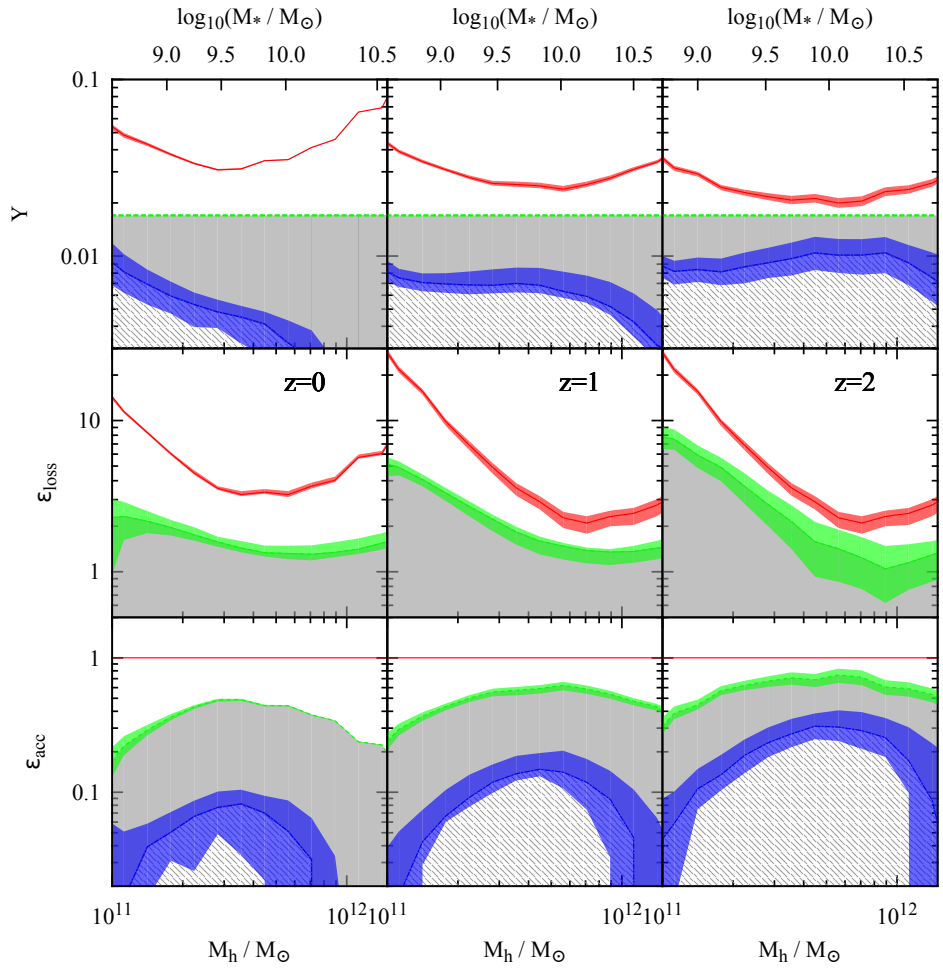

Figure 7. The same as Figure 6 but here the Krumholz star formation model is assumed.

net yield $\mathcal{Y}$ and the mass loading factor $\epsilon_{\rm loss}$ using Eqs. (20) and (21). The results are shown as the red curves in Figure 6 for the Kennicutt-Schmidt star formation model and in Figure 7 for the Krumholz model, respectively. Although the two star formation models lead to sizable differences in the gas mass, the predicted mass loading factors and net yields are very similar, suggesting that this uncertainty does not strongly affect the estimates of the yield and mass loading factor. The reason for this is that the conditions leading to the approximate model given by Eqs. (23) and (24) are valid, so that $\mathcal{E}_{\rm SF}$ and $\mathcal{Y}$ are independent of $M_{\rm g}$. In this case the gas exchange between the galaxy and the environments is rapid. For example, the required loading factor for 10^{11} M$_\odot$ halos can be as high as 10 to 20.

With the use of the fiducial M-Z relations as constraints, the net yield $\mathcal{Y}$ predicted exceeds the intrinsic yield, y (shown as green horizontal lines in the upper panels of Figs. 6 and 7) at least since $z \approx 2$. The value of $\mathcal{Y}$ defined above is related to a number of factors: (i) the intrinsic yield y; (ii) the value of $Z_{\rm w}$ which is determined by how well the metals produced by stars are mixed with the ISM; and (iii) the value of $Z_{\rm r}$ which is determined by the history of the galaxies. In general, the value of $\mathcal{Y}$ cannot exceed that of y because metals in both inflow and outflow must have been diluted. In large scale cosmological simulations (e.g. Dave et al. 2012) and semi-analytic model of galaxy evolution (e.g. Lu Y. et al. 2013), metals produced by stars are assumed to be fully mixed with the ISM, so that $Z_{\rm w} = Z$ is expected. Also, the observed metallicity of the ISM generally increases monotonically with time, so that $Z_{\rm r} < Z$. Putting all these together implies $\mathcal{Y} = y + \epsilon_{\rm r}\,(Z_{\rm r} - Z) < y$. On the other hand, in the case of no wind recycling, as assumed in Lilly et al. (2013), $\mathcal{Y} = y - \epsilon_{\rm r}\,(Z_{\rm w} - Z) \leq y$. Generally, as long as the recycled material is less enriched than the wind, $\mathcal{Y}$ should always be no larger than the intrinsic yield y. Thus, under the assumption that gas accretion follows the accretion of the host dark halos, the gas outflow would be required to be under enriched in

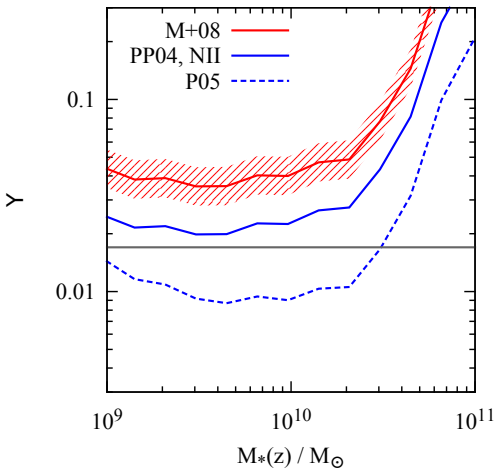

Figure 8. The net yield at $z = 0$ calculated using Eq. (24) assuming $\epsilon_{\rm acc} = 1$. The red solid line is based on the fiducial M-Z relation from Maiolino et al. (2008) and the band indicates the systematic uncertainty from the photoionization modeling. The blue solid line and the blue dashed line are based on the metallicity measurements using the calibrations from Pettini & Pagel (2004) and Pilyugin & Thuan (2005) respectively, both are based on $T_{\rm e}$ method. The horizontal line shows the intrinsic yield.

metals than what is to be expected, suggesting that the assumption $\epsilon_{\rm acc} = 1$ is invalid.

As shown in Eq. (24), the net yield $\mathcal{Y}$ is roughly proportional to the gas phase metallicity measured Z. This provides a simple way to understand the systematic effects in the measured gas phase metallicity. These effects are carefully analyzed in Kewley & Ellison (2008). The variance between different measurements using the photoionization modeling (the second method briefly described in §3) is about 0.2 dex, and the resultant uncertainty in the net yields is shown as the red band shown in Figure 8. It is clear that the net yield $\mathcal{Y}$ required is always larger than the intrinsic value y, in conflict with the expectation that $\mathcal{Y} < y$.

We have also used the M-Z relations derived from the $T_{\rm e}$ method (or calibrations based on this method) to estimate the net yield, and the results are shown as the blue lines in Figure 8. For HII regions with $12 + \log_{10}({\rm O/H}) > 8.6$ the metallicity derived from this method is systematically lower. In particular, the M-Z relation from Pilyugin & Thuan (2005) is lower by 0.7 dex. The values of $\mathcal{Y}$ so derived are consistent with the intrinsic yield from stellar evolutions models, except at the massive end. Unfortunately, this agreement cannot be taken seriously, because theoretical investigations have demonstrated that the $T_{\rm e}$-based methods tend to underestimate the metallicity in metal rich HII regions (e.g. Stasinska 2005). What is clear, though, is that accurate measurements of the gas phase metallicity can provide stringent constraints on galactic inflow and outflow.

5.2 Constraining gas inflow and outflow

As discussed in the previous subsection, the natural assumption that the net yield ought to be lower than the intrinsic yield requires a reduced rate for gas exchange between galaxy and its ambient medium. If the baryon mass exchange is too rapid via inflow of pristine gas or outflow of metal enriched ISM, the predicted gas phase metallicity would be too low when a reasonable value is assumed for the net yield. What this means is that we can constrain the upper limit for the inflow and outflow efficiencies, $\epsilon_{\rm acc}$ and $\epsilon_{\rm loss}$, by setting $\mathcal{Y}$ to its upper limit, namely setting $\mathcal{Y} = y$. It can be shown that, as long as $Z_{\rm w} \geq Z$ and $Z_{\rm w} \geq Z_{\rm r}$, the relation $\mathcal{Y} = y$ requires both $Z_{\rm w} = Z$ and $Z_{\rm w} = Z_{\rm r}$. As mentioned above, $Z_{\rm w} = Z$ implies that the metals produced from star formation is fully mixed with the ISM. In this case, gas outflow is the least efficient in carrying metals out of galaxies. The second condition, $Z_{\rm w} = Z_{\rm r}$, implies that some of the ejected gas is recycled instantaneously while the rest is permanently lost. The upper limits to $\epsilon_{\rm acc}$ so obtained are shown as the green lines in the lower panels of Figs. 6 and 7, while the upper limits to $\epsilon_{\rm loss}$ are shown as the green lines in the middle panels of the same figures.

The two different star formation models produce similar results. The variation in the gas content does not cause much variation in the estimate of $\epsilon_{\rm acc}$. The low star formation efficiency in low-mass galaxies is due to strong outflow at $z = 2$, and to inefficient accretion at $z = 0$. At $z = 2$, the mass loading is roughly proportional to $M_{\rm h}^{-1}$ and is about 10 for 10^{11} M$_\odot$ halos. At $z = 0$ the mass loading depends only weakly on halo mass, with values close to 1. Both the accretion efficiency, $\epsilon_{\rm acc}$, and the effective wind loading factor, $\epsilon_{\rm loss}$, drop by a factor of 2 from $z = 2$ to $z = 0$. These drops are direct results of the evolution in the observed M-Z relation, as our model assumes full mixing. At high redshift, a large fraction of metals are required to be lost with the ejected ISM in order to reproduce the relatively low metallicity, while at low redshift most of the metals are retained so as to reproduce the increased metallicity.

We also consider another special case in which there is no wind recycling, i.e. $\epsilon_{\rm loss} \to 0$. [1] In this case, the accretion efficiency $\epsilon_{\rm acc}$ is required to be much lower than unity in order to maintain the total amount of cold gas in the disk. In this limit, the approximations given by Eqs. (23) and (24) are not valid anymore, and the derived $\epsilon_{\rm acc}$ depends on the star formation models adopted. For instance, since the gas fraction at high z predicted by the Krumholz model is systematically higher than the prediction of the Kennicutt-Schmidt model, the required gas ac-

[1] As shown in the following subsection, outflow of metals is always required to ensure $\mathcal{Y} \leq y$, and so strictly speaking $\epsilon_{\rm loss}$ cannot be exactly zero.

cretion at low redshift is much lower, because the star formation at low redshift can be fueled by the gas accumulated earlier in the galaxy. If reincorporation of ejected gas is taken into account, it is possible that $\epsilon_{\rm loss} < 0$. In this case, the corresponding $\epsilon_{\rm acc}$ and $\mathcal{Y}$ will occupy the grey hatched areas shown Figs. 6 and 7.

The boundaries we draw are based on the fiducial *M-Z* relations and the fiducial intrinsic oxygen yield. As mentioned above, the systematic uncertainty in the metallicity estimate using detailed photoionization modeling is ±0.1 dex around the mean. Since in the full mixing model, which gives the upper limits of $\epsilon_{\rm acc}$ and $\epsilon_{\rm loss}$, the simple proportionality in Eq. (24) holds, a change by ±0.1 dex in metallicity simply leads to a change of ∓0.1 dex in $\epsilon_{\rm acc}$ and to a change of ±0.1 dex in $\epsilon_{\rm loss}$. However, if the $T_{\rm e}$-based metallicity is used as model constraint, the assumption that gas accretion into the galaxy follows the accretion of dark matter, i.e. $\epsilon_{\rm acc} \approx 1$, is still permitted by the metallicity measurements, as shown in Figure 8.

The oxygen yield from Kobayashi et al. (2006) is about 0.01. This number is quite close to the blue lines in the upper panels of Figs. 6 and 7, which are obtained by setting $\epsilon_{\rm loss} = 0$. This suggests that the combination of the Kobayashi et al. (2006) chemical evolution model with the metallicity measurements using detailed photoionization modeling strongly prefers a weak outflow scenario, even at $z \approx 2$.

5.3 Metal loss

The loading factor of metal loss rate $\epsilon_{\rm loss,Z}$ can be directly estimated from Eq. (17), and the estimate is independent of the rates of gas inflow and outflow. Figure 9 shows $\epsilon_{\rm loss,Z}$ as a function of halo mass at three different redshifts. As one can see, net metal outflow is always required, i.e. $\epsilon_{\rm loss,Z} > 0$, for different halos at different redshifts, regardless of the gas outflow. The loading factor predicted with the Kennicutt-Schmidt law is about 0.01, which is about 60% of the yield (indicated by the horizontal lines), and depends only weakly on redshift and the mass of the host halos. This is consistent with the finding of Peeples et al. (2014), that is about 75% of the metals ever produced do not stay in the host galaxies. The prediction using the Krumholz model is similar except that at $z = 2$ the mass loading factor is lower. The reason for this difference is that the Krumholz model predicts higher cold gas fraction at $z = 2$, and so a larger fraction of newly produced metals can be stored in the ISM instead of going out with the wind.

6 CONCLUSIONS AND IMPLICATIONS

In the present paper, we have combined up-to-date observational constraints, including the star formation - halo mass relations (Lu Z. et al. 2014b), the gas phase metallicity - stellar mass relations (Maiolino et al. 2008), and the gas mass fraction of local galaxies (Peeples & Shankar 2011), and used a generic model to investigate how the contents, inflow and outflow of gas and metals evolve in the ecosystem of a low-mass galaxy. The goal is to understand the underlying physics responsible for the low star formation efficiency in halos with masses between $10^{11}\,{\rm M}_\odot$ and $10^{12}\,{\rm M}_\odot$. Our conclusions are summarized in the following.

We adopt both the Kennicutt-Schmidt and the Krumholz models of star formation and combine each of them with the star formation histories of galaxies derived from the empirical model of Lu Z. et al. (2014b) to constrain the gas contents in galaxies up to $z = 2$. We find that (i) The gas mass to stellar mass ratio in general increases with redshift because of the increase of SFR; (ii) The Krumholz model predicts a higher gas mass fraction at high redshift than the

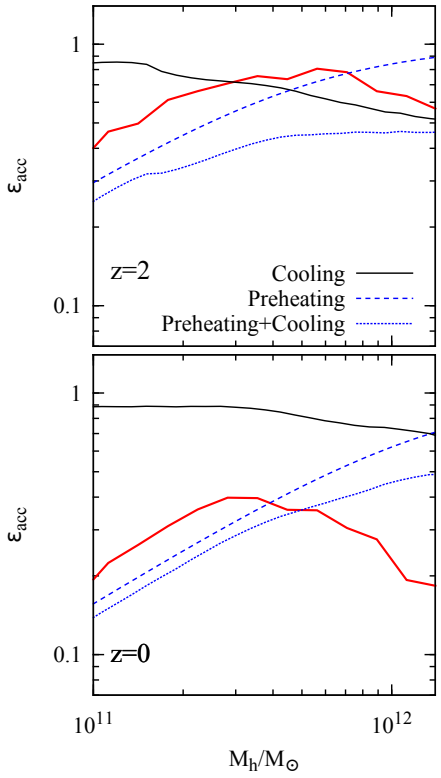

Figure 10. Comparison between the upper limit of the accretion efficiency derived from our empirical model (red lines) with a number of physical models. The black solid lines are cooling efficiency of halo gas (Croton et al. 2006). The blue dashed lines are the efficiency of accretion into dark matter halos in the preheating model of Lu Y. et al. (2014) and the blue dotted lines show the accretion to the galaxies in the same model.

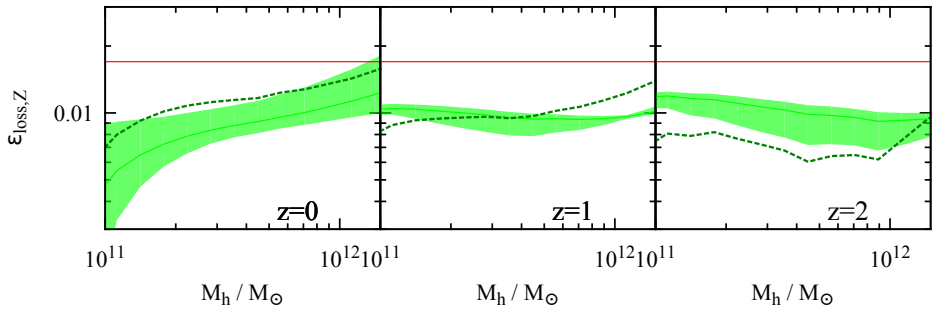

Figure 9. The loading factor of metal loss rate. Light green represents the Kennicutt-Schmidt star formation law and dark green represents the Krumholz star formation model. The curves are the predictions of the best fitting model in Table 2 and the bands are obtained by marginalizing the uncertainties in the parameters. The red horizontal lines are the intrinsic yield of oxygen.

Kennicutt-Schmidt model, especially in dwarf galaxies, because of its dependence on metallicity and because of the metallicity evolution of the ISM; (iii) The Krumholz model predicts that the ISM of galaxies is dominated by the molecular gas at $z > 1$, with the molecular gas to stellar mass ratio increasing from ~ 0.1 at $z = 0$ to ~ 1 at $z = 2$; (iv) The baryon mass ratio, $(M_{\rm g} + M_\star)/M_{\rm h}$, is, since $z = 2$, always much less than the universal baryon mass fraction.

Using the gas mass estimated from the star formation laws together with other observational data, we derive constraints on the gas inflow and outflow rates. Independent of the gas outflow rate, metal outflow is always required at different redshift. The metal mass loading factor is about 0.01, or about 60% of the metal yield, and this factor depends only weakly on halo mass and redshift.

In spite of the degeneracy between gas inflow and outflow, and the uncertainties in modeling how metals are mixed with the medium, we can still put constraints on gas inflow and outflow. As the galactic wind material is expected to be more metal enriched than both the ISM and the material ejected at an earlier epoch, we can derive stringent upper limits on the accretion rate of primordial gas and on the net gas mass loss rate in the outflow. We find that (i) At $z \sim 0$, the low star formation efficiency is mainly caused by the low accretion rate. The maximum loading factor of the mass loss is about one while the maximum accretion efficiency factor $[\dot{M}_{\rm acc}/(f_{\rm b}\dot{M}_{\rm h})]$ is between 0.3 and 0.4; (ii) At $z \sim 2$, strong gas mass loss is allowed. The maximum loading factor allowed by the observational constraints is about 10 for $10^{11}\,{\rm M}_\odot$ halos, and is inversely proportional to halo mass. These upper limits do not depend significantly on the star formation laws adopted, because the exact amount of gas in the galaxies is irrelevant in estimating the rate of gas exchange, as long as $M_{\rm g} \ll f_{\rm b}M_{\rm h}$, which is roughly the case based on our model inferences.

In a typical semi-analytic model of galaxy formation, the mass accretion into a *halo* is usually assumed to be $f_{\rm b}\dot{M}_{\rm h}$, and the mass accretion into the *central galaxy* is determined by the cooling rate of the gaseous halo. Following the cooling model of Croton et al. (2006) (also in Lu Y. et al. 2011) and assuming a metallicity of $0.1Z_\odot$ in the coronal gas, we calculate the efficiency of mass accretion in such a process, and the value of $\epsilon_{\rm cool} \equiv \dot{M}_{\rm cool}/(f_{\rm b}\dot{M}_{\rm h})$ is shown as the black solid lines in Figure 10. We see that $\epsilon_{\rm cool} \sim 1$ for a $10^{11}\,{\rm M}_\odot$ halo, and is roughly proportional to $M_{\rm h}^{-0.2}$ in the halo mass range shown in the figure. At $z = 2$ $\epsilon_{\rm cool}$ is close to the upper limit of $\epsilon_{\rm acc}$ we have derived, but at $z = 0$ it is significantly larger. The discrepancy between this prediction and our empirically derived constraint suggests that either accretion of the IGM into dark halos must be reduced or the cooling of the halo gas must be slowed down.

The scenario of galaxy formation in a preheated medium was first proposed in Mo & Mao (2002) in order to explain the observed stellar mass functions and HI mass function. Lu Y. et al. (2014) suggested that the extended gas disks provide independent supports to such a scenario. They considered an "isentropic" accretion model, in which the IGM is assumed to be preheated to a certain level at $z < 2$ so that the gas accretion rate into low-mass halos is reduced. The hot gaseous halos formed in this way are less concentrated and cooling can happen even in the outer part of a halo, where the specific angular momentum is higher, producing a disk size - stellar mass relation that matches observation. Using the entropy model explored in Lu Y. et al. (2014) we have calculated the accretion efficiency of the pre-heated IGM into *dark matter halos*, which is shown as the blue dashed lines in Figure 10. The corresponding accretion rate of the central galaxies due to radiative cooling of the gaseous halos is shown as the blue dotted lines. At $z = 2$, the accretion efficiency lies below the upper limit, and so the model is compatible with our results. At $z = 0$, the predicted accretion efficiency is consistent with

the upper limit we obtained for halos with masses below $4 \times 10^{11}\,M_\odot$ but is higher by a factor of ~ 2 for Milky Way mass halos.

It is still unclear how the IGM is preheated. In addition to the possibilities listed in §1, Lu Z. & Mo (2014c) proposed that intermediate mass central black holes can serve as a promising source. According to Lu Z. & Mo (2014c), such black holes form from the major merger between dwarf galaxies at $z > 2$ and is able to heat the surrounding IGM to a entropy tested in Lu Y. et al. (2014).

For Milky Way mass halos, preventing the IGM from collapsing with the dark matter requires an entropy level that is much larger than what Lu Y. et al. (2014) suggests. Such a high level of preheating may over-quench star formation in smaller galaxies. It is more likely that some other *preventive* (rather than ejective) mechanisms may reduce *gas cooling* in such galaxies at low redshift, instead of preventing gas accretion into the *host halo*. For example, a central black hole may keep halo gas hot via the "radio mode" feedback, preventing it from further cooling (Croton et al. 2006). Clearly, it is important to examine if such "radio mode" feedback is also operating in Milky Way size galaxies, or other processes have to be invoked. Using hydrodynamic simulation of Milky Way mass galaxies, Kannan et al. (2014) found that the ionizing photons from local young and aging stars can effectively reduce the cooling of the halo gas, which may provide another promising preventive mechanism to reduce star formation efficiency in such galaxies at low redshift, as predicted by our empirical model

ACKNOWLEDGEMENTS

We thank Frank van den Bosch for helpful comments. HJM would like to acknowledge the support of NSF AST-1109354.

REFERENCES

Asplund Martin, Grevesse Nicolas, Sauval A. Jacques & Scott Pat, 2009, ARA&A, 47, 481
Baldry I.K. et al. 2012, MNRAS, 421, 621
Behroozi P.S., Conroy C., Wechsler R.H., 2010, ApJ, 717, 379
Behroozi P.S., Wechsler R.H., Conroy C., 2013, ApJ, 762, 31
Béthermin M., et al. 2013, preprint, arXiv1304.3936
Boselli A., Cortese L., Boquien M., Boissier S., Catinella B., Lagos C. & Saintonge A., 2014, A&A, 564, 66
Bouche N., Dekel A., Genzel R., Genel S., Cresci G., Forster Schreiber N.M., Shapiro K.L., Davies R.I. & Tacconi L., 2010, ApJ, 718, 1001
Bruzual G. & Charlot S., 2003, MNRAS, 344, 1000
Chabrier G., 2003, PASP, 115, 763
Chang P., Broderick A. & Pfrommer C., 2011, arXiv:1106.5504
Cole S., Helly J., Frenk C. S., Parkinson H., 2008, MNRAS, 383, 546
Conroy C., Wechsler R.H. & Kravtsov A.V., 2006, ApJ, 647, 201
Conroy C. & Wechsler R.H., 2009, ApJ, 696, 620
Croton D.J., et al., 2006, MNRAS, 365, 11
Cantalupo Sebastiano, 2010, MNRAS, 403, 16
Dalcanton Julianne J., 2007, ApJ, 658, 941
Dave R., Finlator K. & Oppenheimer B.D., 2012, MNRAS, 421, 98
Dave Romeel, Katz Neal, Oppenheimer Benjamin D., Kollmeier Juna A. & Weinberg, David H., 2013, MNRAS, 434, 2645
Dekel A. & Silk J., 1986, ApJ, 303, 39
Dutton A., van den Bosch F. C. & Dekel A., 2010, MNRAS, 405, 1690
Dutton A. et al., 2011, MNRAS, 410, 1660
Erb Dawn K., Shapley Alice E., Pettini Max, Steidel Charles C., Reddy Naveen A. & Adelberger Kurt L., 2006, ApJ, 644, 813
Erb D., 2008, ApJ, 674, 151
Feldmann R., 2013, MNRAS, 433, 1910
Gnedin N., 2000, ApJ, 542, 535
Henry Alaina, Martin Crystal L., Finlator Kristian & Dressler Alan, 2013, ApJ, 769, 148
Ikeuchi S., 1986, Ap&SS, 118, 509
Jiang F., van den Bosch F.C., 2014, MNRAS, in press (arXiv:1311.5225)
Kannan R., Stinson G. S., Maccio A. V., Hennawi J. F., Woods R., Wadsley J., Shen S., Robitaille T., Cantalupo S., Quinn T. R. & Christensen C., 2014, MNRAS, 437, 2882
Kobayashi Chiaki, Umeda Hideyuki, Nomoto Kenichi, Tominaga Nozomu & Ohkubo Takuya, 2006, ApJ, 653, 1145
Kennicutt R.C. Jr, 1998, ApJ, 498, 541
Kewley L. & Ellison S., 2008, ApJ, 681, 1183
Komatsu et al., 2011, ApJS, 192, 18
Kravtsov Andrey V., 2013, ApJL, 764, 31
Krumholz M. & Dekel A., 2012, ApJ, 753, 16
Krumholz M. R., McKee C. F. & Tumlinson J., 2008, ApJ, 689, 865
Krumholz M. R., McKee C. F. & Tumlinson J., 2009, ApJ, 693, 216
Leroy Adam K., Walter Fabian, Brinks Elias, Bigiel Frank, de Blok W. J. G., Madore Barry & Thornley M. D., 2008, AJ, 136, 2782
Lilly Simon J., Carollo C. Marcella, Pipino Antonio, Renzini Alvio & Peng Yingjie, ApJ, 2013, 772, 119
Lu Y. & Mo H. J., 2007, MNRAS, 377, 617
Lu Yu, Keres Dusan, Katz Neal, Mo H. J., Fardal Mark & Weinberg Martin D., 2011, MNRAS, 416, 660
Lu Y. et al., 2013, arXiv1312.3233
Lu Y., Mo H. J. & Wechsler, Risa H., 2014, arXiv1402.2036
Lu Z., Mo H.J., Lu Y., Katz N., Weinberg M. D.,

van den Bosch F. C. & Yang X., 2014a, MNRAS, 439, 1294
Lu Z., Mo H.J., Lu Y., Katz N., Weinberg M. D., van den Bosch F. C. & Yang X., 2014b, arXiv1406.5068
Lu Z. & Mo H.J., 2014, arxiv1407.4382
Mac Low M. & Ferrara A., 1999, ApJ, 513, 142
Maiolino R., Nagao T., Grazian A., et al. 2008, A&A, 488, 463
Mo H.J. & Mao S., 2002, MNRAS, 333, 768
Mo H.J. & Mao S., 2004, MNRAS, 353, 829
Mo H.J., Yang X., van den Bosch F.C. & Katz N., 2005, MNRAS, 363, 1155
Moster B.P., Somerville R.S. Maulbetsch C., van den Bosch F.C., Maccio A.V., Naab T., Oser L., 2010, ApJ, 710, 903
Neistein E. & Weinmann S.M., 2010, MNRAS, 405, 2717
Oppenheimer B. D. & Dave R., 2008, MNRAS, 387, 577
Papastergis Emmanouil, Cattaneo Andrea, Huang Shan, Giovanelli Riccardo & Haynes Martha P., 2012, ApJ, 759, 138
Parkinson H., Cole S. & Helly J., 2008, MNRAS, 383, 557
Peimbert M. & Costero R., 1969, BOTT, 5, 3
Pettini M. & Pagel B. E. J. 2004, MNRAS, 348, 59 (PP04)
Pilyugin L. S. & Thuan T. X. 2005, ApJ, 631, 231 (P05)
Peeples M. & Shankar F., 2011, MNRAS, 417, 2962
Peeples M. S., Werk J. K., Tumlinson J., Oppenheimer B. D., Prochaska J. X., Katz N. & Weinberg D. H., 2014, ApJ, 786, 54
Popesso P., Biviano A., Bohringer H. & Romaniello M., 2006, A&A, 445, 29
Popping G., Caputi K. I., Somerville R. S. & Trager S. C., 2012, MNRAS, 425, 2386
Popping G., Somerville R. S. & Trager S. C., 2014, MNRAS, 442, 2398
Portinari L., Chiosi C. & Bressan A., 1998, A&A, 334, 505
Rees M. J., 1986, MNRAS, 218, 25
Santini et al., 2012, AA, 538, 33
Stasinska G., 2005, A&A, 434, 507
Tacconi L.J. et al., 2013, ApJ, 768, 74
Tremonti et al., 2004, ApJ, 613, 898
van den Bosch F.C., Yang X., Mo H.J., 2003, MNRAS, 340, 771
van de Voort F., Schaye J., Booth C. M., Haas M. R. & Vecchia C. D., 2011, MNRAS, 414, 2458
van der Wel A. et al., 2014, ApJ, 788, 28
Yang X., Mo H.J. & van den Bosch F., 2003, MNRAS, 339, 1057
Yang X., Mo H.J., van den Bosch F.C., Zhang Y., Han J., 2012, ApJ, 752, 41
Yang X., Mo H.J., van den Bosch F.C., Bonaca A., Li S., Lu Y., Lu Y., Lu Z., 2013, ApJ, 770, 115
Zahid H. Jabran, Geller Margaret J., Kewley Lisa J., Hwang Ho Seong, Fabricant Daniel G. & Kurtz Michael J., 2013, ApJ, 771, 19
Zahid H. Jabran, Torrey Paul, Vogelsberger Mark, Hernquist Lars, Kewley Lisa & Dave Romeel, 2014, Ap&SS, 349, 873